



Coupled aerodynamic and hydrodynamic response of a long span bridge suspended from floating towers

Jungao Wang^{a,*}, Etienne Cheynet^a, Jónas Þór Snæbjörnsson^{a,b}, Jasna Bogunović Jakobsen^a

^a Department of Mechanical and Structural Engineering and Materials Science, University of Stavanger, N-4036 Stavanger, Norway

^b School of Science and Engineering, Reykjavík University, IS-101 Reykjavík, Iceland



ARTICLE INFO

Keywords:
Floating bridge
Time domain
Coupled analysis
Turbulent wind
Inhomogeneous waves
Finite element analysis

ABSTRACT

The present study introduces a fully coupled time-domain analysis of a multi-span suspension bridge supported by two floating towers, considered for crossing the wide and deep fjords along the west coast of Norway. The time-domain analysis is performed with a finite element model considering simultaneously the turbulent wind, irregular inhomogeneous ocean waves and sheared ocean current. The numerical results suggest that under extreme conditions with a return period of 100 years, the bridge horizontal response is dominant and governed by the low-frequency modes. For the vertical and torsional responses, the largest contributions are due to the respective motion components of the low-frequency horizontal motion-dominated modes. The investigation into the significance of the aerodynamic and hydrodynamic load reveals that in the case studied, over 80% of the bridge girder response is due to the aerodynamic excitation. The hydrodynamic loads acting on the floating towers are small due to a relatively small significant wave height in the fjord and the counteracting aerodynamic damping effect. By considering the inhomogeneity of the waves, i.e. different conditions at the two floating supports, the contribution of the aerodynamic action to the lateral, vertical and torsional dynamic responses increases by 6%, 7% and 9% respectively.

1. Introduction

The Norwegian Public Road Administration (NPRA) is considering suspension bridges on floating foundations as one of the feasible concepts to cross the deep (0.5–1.2 km) and wide fjords (up to 5 km) in Western Norway (Samferdselsdepartement, 2017). Such bridges will have eigen-frequencies as low as 0.01 Hz and will thus be extremely sensitive to wind loading. In addition, the floating tower supports will be excited by the hydrodynamic loading, so that the floating bridge structural analysis becomes a fully coupled aero-hydrodynamic problem.

The buffeting theory introduced more than 50 years ago by Davenport (1961) and further developed by e.g. Scanlan (1978) is a standard approach to evaluate the bridge dynamic response due to wind turbulence, which is one of the governing design factors for a long-span bridge in the ultimate limit state (ULS). The estimation of the buffeting response has been extensively studied in both the frequency-domain (Biety et al., 1995; Lin and Yang, 1983; Macdonald, 2003; Xu and Zhu, 2005), and the time-domain (Aas-Jakobsen and Strømmen, 2001; Borri et al., 1995; Chen et al., 2000; Costa et al., 2007; Diana et al., 2008; Svensson and Kovacs, 1992; Wang et al., 2010). The estimated buffeting response has

further been attempted to be validated through full-scale measurements (Biety et al., 1995; Cheynet et al., 2016; Fenerci and Øiseth, 2017; Macdonald, 2003; Wang et al., 2010; Xu and Zhu, 2005). The global hydrodynamic analysis of a single offshore structural system like a tension-leg platform (TLP), comprising slender structural elements like tethers and risers, is a relatively standard procedure according to design guidelines (DNV, 2010, 2011), which has been investigated extensively in frequency-domain and time-domain numerical simulations (Bachynski, 2014; Kim et al., 2001; Masciola, 2011). Additionally, there are topics like higher-order wave forces (e.g. springing and ringing loads), which are challenging to predict accurately in numerical simulations due to their strongly non-linear nature (Faltinsen et al., 1995; Gurley and Kareem, 1998; Marino et al., 2015; Paulsen et al., 2014). These higher-frequency loads are however essential for predicting fatigue life of TLP tendons and risers (Bachynski and Moan, 2014; Petruskas and Liu, 1987). There are also other load components, like the low-frequency drift damping of the TLP hull and the viscous damping of the slender structures, which should preferably be validated or determined through experiments (DNV, 2010).

For a floating bridge concept devised to cross deep and wide fjords, a

* Corresponding author.

E-mail address: jungao.wang@uis.no (J. Wang).

recent design basis report (Borge et al., 2015) describes the co-existence of the wind, the wind-generated waves, swells and ocean current in one of the Norwegian fjords. Because of the local fjord topography, both wind-generated waves and swells, have a significant wave height and period that varies across the fjord, the wave conditions are defined as inhomogeneous. For the case of the Sulafjord studied in this paper, the islands outside the fjord provide wave sheltering effects. Accordingly, the significant wave height will be much larger at the northeast side of the fjord than at the southwest. The inhomogeneity of the waves should thus be considered when assessing the wave load effects. It is also important to account for the combined simultaneous aerodynamic and hydrodynamic actions, to properly include the structural motion-dependent loads. The motion-dependent loads comprise the self-excited aerodynamic forces on the bridge superstructure and the motion-induced hydrodynamic forces on the floater and the slender structural elements connecting the floater to the seabed. Due to the complexity and novelty of such a megastructure, there is a limited literature available on the coupled analysis considering large volume floater hydrodynamics, slender structure hydrodynamics and bridge aerodynamics. Nesteby et al. (2015) performed a feasibility study on the concept of a multi-span floating suspension bridge for the Sulafjord, in which the bridge response under separated aerodynamic and hydrodynamic actions was calculated by using two different software packages. The simple transfer functions between the wind/wave excitation and the bridge response were constructed to address the combined load effect. However, the coupling effect of the aerodynamic and hydrodynamic loads is neglected. Lie et al. (2016) used the software package SIMO/Riflex/SIMA for preliminary feasibility studies on different floating bridge concepts, where the wind action is simplified as a static load and only the homogeneous wave condition can be specified in SIMO. Wei et al. (2017) proposed a frequency domain hydroelasticity method in which the continuous floating structure was discretized into rigid modules connected by elastic beams, and inhomogeneous wave conditions at different module were applied individually. The results indicate that the inhomogeneity of the regular waves may induce larger maximum vertical bending moment to the structure compared to a homogeneous wave field along the structure.

This paper focuses on the overall bridge response under extreme environmental conditions, as well as the contributions from different excitation sources, to reveal the dominant design action for a floating bridge of this type. For this purpose, a fully coupled aero-hydrodynamic numerical tool is developed. A finite element model is integrated with a

load model considering the simultaneous excitation from turbulent wind, inhomogeneous irregular ocean waves and the sheared ocean current.

2. The floating bridge concept and environmental conditions

2.1. The Sulafjord site

The case studied concerns a bridge across the Sulafjord, between the islands of Hareidlandet and Sula in Møre and Romsdal County. As illustrated by the elevation map in Fig. 1, which has been digitally evaluated based on the Shuttle Radar Topography Mission (SRTM) database (Farr et al., 2007), there are mountains on both sides of the fjord, with altitudes up to 700 m. At the northwest side of the fjord, the Godøya island, with an altitude of 400 m, is sheltering the fjord to some extent from the open ocean. To the southeast, there is a mountainous area with altitudes above 1000 m. One of the proposed concepts for the fjord crossing is a multi-span bridge suspended from two fixed towers and two towers on the floating foundations (Nesteby et al., 2015). The blue line segment across the Sulafjord in Fig. 1 shows the proposed location of floating bridge, where the fjord is around 4.5 km wide and 450 m deep.

2.2. Floating bridge structural properties

Fig. 2 presents the finite element (FE) model of the floating bridge, which gives an overview of the bridge design and structural components. The bridge consists of three main spans and two side spans suspended

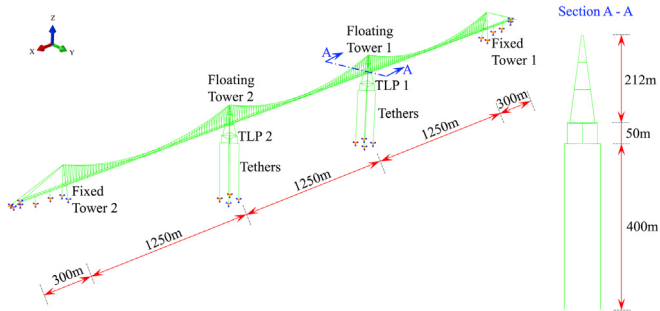


Fig. 2. The Sulafjord floating bridge model, as plotted in Abaqus (ABAQUS, 2011).

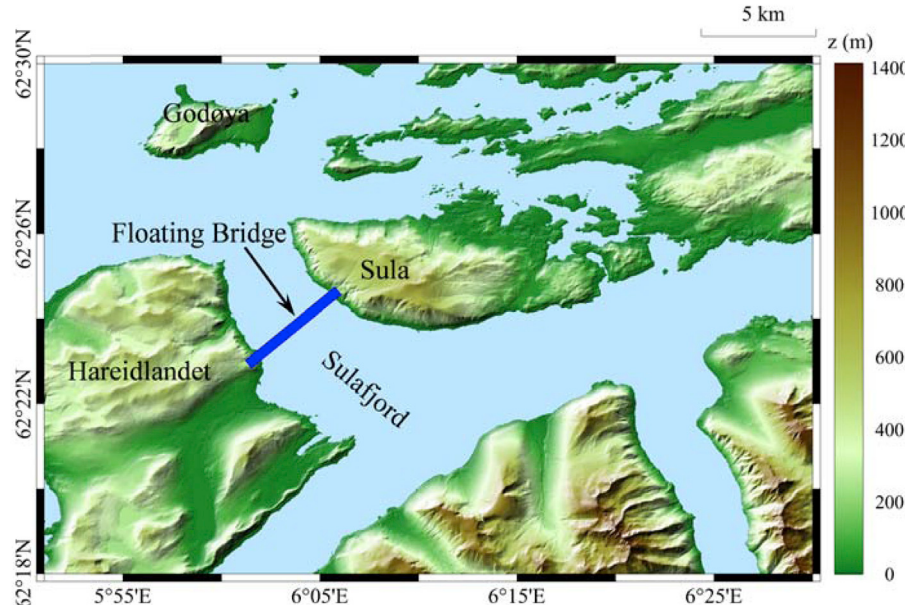


Fig. 1. Elevation map of the Sulafjord site on the west coast of Norway including the bridge location.

Table 1

Structural and aerodynamic properties of the Sulafjord bridge.

	Girder	Main cables	Hangers	Floating tower leg	Fixed tower leg
Dimensions	B x H/D (m)	30x3.6	0.7	5x5	7x5
Area	A (m^2)	1.127	0.3	0.912	1.104
Mass	M (10^3 kg/m)	16.5	2.36	0.056	8.67
Modulus	E (GPa)	210	195	165	210
Moment of inertia	I _x (m^4)			3.71	4.88
	I _y (m^4)	2.32		3.71	8.11
	I _z (m^4)	81.57			
	I _r (m^4)	5.08		5	8.17
	I _m ($10^3 \text{ kgm}^2/\text{m}$)	1093			
Aerodynamic coefficients	C _D	0.80	0.82	0.85	1.52
	C' _D	0			
	C _L	−0.20			
	C' _L	4.30			
	C _M	0.02			
	C' _M	0.92			

from two floating towers and two fixed towers. The length of the main spans is 1250 m and the side spans are 300 m long. The bridge girder, standing 85 m above the sea level, is designed as a streamlined single closed steel box. Both the fixed and floating tower reach an elevation of 212 m in a pyramidal configuration, as illustrated by the sectional view in Fig. 2. Because of the tower shape, the distance between the two main cables varies between 4 m at the top of the tower and about 26 m at the mid-span. The main cable has a vertical sag of 125 m, which is equal to 1/10 of the main span. The adjacent hangers are 20 m apart. Further details of the overall design and structural properties, based on the Multiconsult report (Nestebø et al., 2015), are summarized in Table 1, which also includes the static aerodynamic coefficients. Only the drag load is considered for the main cables, the hangers and the towers.

Below the waterline, each floating tower is sitting on top of a TLP, with four circular columns connected to four rectangular pontoons at the bottom with a draft of 50 m. The dimensions and hydrodynamic properties of the TLP are summarized in Table 2. At each corner of the TLP, there are four tethers connected to the seabed, 450 m below the sea level. The 16 tethers provide a total pre-tension of 250 MN to the TLP.

2.3. Environmental conditions

The topography at the Sulafjord site is rather complex, with islands, mountainous areas and open ocean close by. At present, the on-site measurement data of the wind, wave and current conditions are limited. The extreme wind-driven waves and swells under the return periods of 10 years, 100 years and 10000 years have been estimated by Multiconsult based on a two-dimensional semi-empirical wave model (Borge et al., 2015). According to their report, more severe wind-driven waves and swells are expected along the northeast coast of the fjord compared to those at the southwest side.

Three sets of load modelling parameters representing different environmental conditions with a return period of 100 years are considered in the present numerical simulations to understand the ultimate limit state (ULS) of the proposed floating bridge concept. The parameters are summarized in Table 3. Environmental condition 1 assumes that both

wind-waves and swells are uncorrelated and are characterized by higher significant wave heights at TLP1 than at TLP2, according to the metocean design basis (Borge et al., 2015). Environmental condition 2 assumes the wind-waves are fully uncorrelated, but the swells are fully correlated at both TLPs. Environmental condition 3 assumes both wind-wave and swells are fully correlated at two locations. It should be mentioned that the wave correlation in environmental conditions 2 and 3 may not be fully representative of the real wave conditions in the fjord. However, the numerical cases selected for the analysis allow us to better understand how the inhomogeneity of the waves affects the response of a floating bridge of this type. More realistic environmental conditions rely on the local metocean condition survey which is ongoing, operated by Fugro OCEANOR AS.

The wave correlation is controlled by the random seed parameter when generating the wave time histories. Five realizations are simulated in time domain for environmental condition 1 and the results are averaged. For environmental condition 2 and 3, the waves are different from condition 1, but the wind field is the same as one of the five cases (realizations) simulated for condition 1 to make sure the response differences only depend on the waves.

The combination of actions used herein assumes that the wind-wave, swell, current and wind, all occur at the same time with the same incident angle, i.e. perpendicular to the bridge deck, as a worst-case scenario, named as the “Fully coupled” simulation:

- **Fully coupled:** Wind, wave and current loads applied in an integrated, coupled analysis;

To further investigate the aerodynamic and hydrodynamic actions on the bridge response, two supplementary simulations are analysed, termed as:

- **Aero only:** Buffeting wind loads acting on the bridge, accounting for the motion-induced aerodynamic loads, hydrodynamic radiation forces on the TLPs and tethers only, but no hydrodynamic excitation forces;

Table 2

Structural and hydrodynamic properties of the TLP and tethers.

TLP	Tethers		
Mass (ton)	3.4E4	Length (m)	400
Center of gravity (m)	−39	Outer diameter (m)	1
Draft (m)	50	Thickness (m)	0.035
Outer diameter of the column (m)	20.5	Arrangement	4 × 4
Space between adjacent column centres (m)	71.5	Total pretension (N)	2.5E8
Width and height of the pontoon (m)	14 × 10	C _D	0.7
C _D of the column	0.487	C _a	1
C _D of the pontoon	2		

Table 3

Environmental condition parameters adopted for the numerical analysis.

	Wind-wave				Swell				Current		Wind
	TLP1		TLP2		TLP1		TLP2		TLP1	TLP2	
	H_s (m)	T_p (s)	V_{top} (m/s)	V_{top} (m/s)							
Environmental condition 1	2.4	7.9	1.6	3.7	2	17	0.9	15	1	1	N400
Environmental condition 2	2	7	2	7	2	17	2	17	1	1	Category 0
Environmental condition 3	2	7	2	7	2	17	2	17	1	1	$V_{b,100} = 31 \text{ m/s}$

Note: H_s is the significant wave height; T_p is the spectral peak wave period; V_{top} is the current velocity at the waterline level; $V_{b,100}$ is the mean wind speed at the reference height (10 m) under the return period of 100 years.

- *Hydro only*: Hydrodynamic loads on the TLPs and tethers only, without any aerodynamic loads.

Table 4 summarizes all the numerical cases simulated in this paper.

The wind-waves and the swells are simulated based on the Jonswap spectrum (Hasselmann et al., 1973).

$$S(\omega) = \frac{\alpha g^2}{\omega^5} \exp \left[-\beta \left(\frac{\omega_p}{\omega} \right)^4 \right] \gamma \exp \left[-\frac{(\omega - \omega_p)^2}{2\sigma^2 \omega_p^2} \right] \quad (1)$$

where α is the spectral parameter which defines the intensity of the spectra, with a typical form shown in Eq. (2) (DNV, 2014); β is the form parameter equal to 1.25; γ is the peak enhancement factor, here set equal to 3.3; ω_p is the angular spectral peak frequency, which can be calculated by $\omega_p = 2\pi/T_p$; σ is the spectral parameter with default values given in Eq. (3).

$$\alpha = 5(1 - 0.287 \ln(\gamma)) \left(\frac{H_s \omega_p^2}{4g} \right)^2 \quad (2)$$

$$\sigma = \begin{cases} 0.07 & \omega < \omega_p \\ 0.09 & \omega > \omega_p \end{cases} \quad (3)$$

Long-crested waves are generated in time-domain based on a spectral representation approach. The ocean current is assumed identical and stationary at both TLP locations, with a linear decrease from 1 m/s at the sea surface to 0 at the seabed 450 m below the sea surface.

As for the wind field characteristics, the semi-empirical wind model recommended by Norwegian Public Roads Administration (NPRA) Handbook N400 (Vegvesen, 2015) is selected to simulate the turbulent wind field, using the method proposed by Shinouka and Deodatis (1991). Time series of the along-wind and vertical wind velocity components are generated in a two-dimensional irregular grid, fixed in space, the nodes of which coincide with the nodes of the motionless bridge structure. The simulation time is, consequently, significantly reduced compared to the case of a more classical regular rectangular grid (Jonkman and Kilcher, 2012), since the number of nodes is greatly reduced. Note that to keep a low discrepancy between the target and simulated power spectral densities, the cell of the grid must not be too large. For this reason, wind velocity data were also generated in some “dummy” nodes between the floating towers.

According to N400, the normalized wind spectrum is:

$$\frac{fS(f)_i}{\sigma_i^2} = \frac{A_i \hat{f}_i}{(1 + 1.5A_i \hat{f}_i)^{5/3}} \quad ; \quad i = u, v, w \quad (4)$$

Table 4
A summary of the numerical cases.

	Condition 1	Condition 2	Condition 3
Fully coupled	5 cases	1 case	1 case
Aero only	5 cases		
Hydro only	5 cases	1 case	1 case

where $\frac{fS(f)_i}{\sigma_i^2}$ is the non-dimensional power spectrum; u, v, w denote the along-wind, across-wind and vertical wind components; $S(f)_i$ is the Power Spectral Density (PSD) of the turbulence at a frequency f ; σ_i is the standard deviation of the wind turbulence component i ; A_i is the empirical parameter representing the along (u), across (v) or vertical (w) wind components, $A_u = 6.8$; $A_v = A_w = 9.4$; \hat{f}_i is the non-dimensional frequency expressed as:

$$\hat{f}_i = \frac{f L_i^x(z)}{\bar{U}(z)} \quad (5)$$

where $L_i^x(z)$ is the height-dependent turbulence length scale in the along-wind direction, which represents the “average gust size”; $\bar{U}(z)$ is the height-dependent mean wind velocity. The mean wind velocity $\bar{U}(z)$ is calculated as:

$$\bar{U}(z) = U_{ref} \kappa_T \ln(z/z_0) \quad (6)$$

where U_{ref} is the reference mean wind velocity at the height of 10 m; κ_T is the terrain factor, which is the ratio of the surface roughness and the von Kármán constant; z_0 is the roughness length, which defines the terrain category.

The length scales for different wind turbulence components in Eq. (5) can be expressed as:

$$L_u^x(z) = \begin{cases} L_1(z/z_1)^{0.3} & ; z > z_{min} \\ L_1(z_{min}/z_1)^{0.3} & ; z \leq z_{min} \end{cases}$$

$$L_v^x(z) = \frac{1}{4} L_u^x(z)$$

$$L_w^x(z) = \frac{1}{12} L_u^x(z) \quad (7)$$

where L_1 is the reference length scale, equal to 100 m; z_1 is the reference height equals to 10 m. z_{min} is an arbitrary minimal height that depends on the terrain category.

The turbulence intensities for different wind components are defined as:

$$I_u(z) = \frac{\sigma_u(z)}{\bar{U}(z)} = \begin{cases} c_{ut}/\ln(z/z_0) & ; z > z_{min} \\ c_{ut}/\ln(z_{min}/z_0) & ; z \leq z_{min} \end{cases}$$

$$I_v(z) = \frac{\sigma_v(z)}{\bar{U}(z)} = \frac{3}{4} I_u(z) \quad (8)$$

$$I_w(z) = \frac{\sigma_w(z)}{\bar{U}(z)} = \frac{1}{2} I_u(z)$$

where c_{ut} is a turbulence factor that depends on the terrain category, taken as 0 for cases simulated herein, according to the wind measurement results at another Norwegian fjord (Cheynet et al., 2017).

Besides the single-point wind statistics described above, the correla-

tion of turbulence along the structure is also fundamental to access the wind load on the entire structure. According to N400, the co-coherence function of turbulence components at two points separated by a distance, d_j , is defined as:

$$\gamma(f, d_j) = \frac{\text{Re}[S_{i_1, i_2}(f, d_j)]}{\sqrt{S_{i_1}(f) \cdot S_{i_2}(f)}} = \exp\left(-C_{ij} \frac{f d_j}{U(z)}\right); \quad i = u, v, w; \quad j = y, z \quad (9)$$

where $\gamma(f, d_j)$ is the co-coherence, which is a function of the frequency f and the Euclidian distance d_j ; $S_{i_1}(f)$ and $S_{i_2}(f)$ are the underlying single point power spectral densities of the turbulence i -components (along-wind, cross-wind or vertical); $S_{i_1, i_2}(f, d_j)$ is the co-spectrum of turbulence at two different points. The co-coherence function decays with an increasing frequency and an increasing distance between the two points considered. According to N400, the coefficients C_{ij} which govern the co-coherence exponential decay are set equal:

$$C_{uy} = C_{uz} = 10; \quad C_{vy} = C_{vz} = C_{wy} = 6.5; \quad C_{wz} = 3 \quad (10)$$

Under the return period of 100 years, the reference 10-min mean wind velocity is 31 m/s at 10 m height. The simulated wind field has a mean wind velocity of 50 m/s at the bridge girder level (85 m) with the along-wind turbulence intensity of 9.6% and vertical turbulence intensity of 4.7%.

3. Numerical methodology

3.1. Wind load model

The wind load due to turbulence as well as the wind-structure interaction are modelled using the quasi-steady approach, i.e. are solely based on the static aerodynamic coefficients (given in Table 1). This approach, adopted in the first stage of the development of a complex numerical model, is plausible considering the expected dominance of the very low-frequency response components. Fig. 3 illustrates the wind force components in the bridge-based coordinate system:

The instantaneous wind-girder angle includes two parts: the torsional displacement r_x and the instantaneous angle α due to the wind turbulence. Fig. 3 uses the same right-hand coordinate as that in Abaqus, therefore, r_x and \dot{r}_x are positive anti-clockwise. This has been considered when calculating the associated forces in Eq. (11). Therefore, the associated drag, lift and overturning moment at the girder shear center can be expressed as

$$\begin{bmatrix} F_D(t) \\ F_L(t) \\ M_x(t) \end{bmatrix} = \frac{1}{2} \rho U_{tot}^2(t) B \begin{bmatrix} H(C_D + C'_D(\alpha(t) - r_x(t))) \\ C_L + C'_L(\alpha(t) - r_x(t)) \\ B(C_M + C'_M(\alpha(t) - r_x(t))) \end{bmatrix} \quad (11)$$

where the instantaneous effective wind velocity $U_{tot}(t)$ can be calculated by

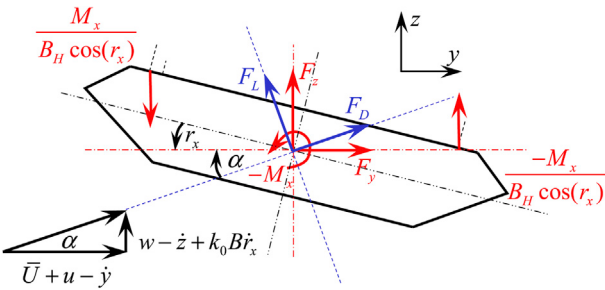


Fig. 3. Force components of the bridge girder cross section subjected to wind load.

$$U_{tot}^2(t) = (\bar{U} + u(t) - \dot{y}(t))^2 + (w(t) - \dot{z}(t) + k_0 B \dot{r}_x(t))^2 \quad (12)$$

As Eq. (12) indicates, the motion-dependent wind load includes a torsional damping term referring to $k_0 B$, where k_0 is the horizontal distance between the aerodynamic center and the shear center normalized by the bridge deck width B , set equal to 0.25 in the present study. The drag and lift forces in Eq. (11) are decomposed into horizontal and vertical components:

$$\begin{bmatrix} F_y(t) \\ F_z(t) \end{bmatrix} = \begin{bmatrix} \cos(\alpha(t)) & -\sin(\alpha(t)) \\ \sin(\alpha(t)) & \cos(\alpha(t)) \end{bmatrix} \cdot \begin{bmatrix} F_D(t) \\ F_L(t) \end{bmatrix} \quad (13)$$

The overturning moment is applied by a pair of vertical forces at the hanger connection points, as illustrated in Fig. 3, with the force magnitude equals to:

$$F_{Hy}(t) = \frac{M_x(t)}{B_H \cos(r_x(t))} \quad (14)$$

Eqs. (11)–(14) are the full expressions of the applied wind buffeting forces in time-domain. It can be observed that all the three force components in Eq. (11) have time-dependent elements on the right-hand side of the equations, which are related to the girder motion terms. For the cable, hanger and tower elements, only the mean and the fluctuating drag forces are considered, using a similar approach as that for the girder. The wind-induced buffeting loads are calculated at each time step through a user-defined subroutine in Abaqus considering the relative wind velocity and the instantaneous angle of attack. The feasibility and accuracy of this time-domain scheme in Abaqus for wind-induced bridge buffeting response analysis have been investigated for the in-service Lysefjord Bridge in Norway, where the numerical simulation results were found to be consistent with the monitored full-scale bridge vibration response (Wang et al., 2017).

3.2. Floater and tether hydrodynamic load model

For the TLP, which is a large volume floater, the hydrodynamic analysis is performed in the frequency-domain using HydroD (2005) to calculate the first-order frequency-dependent wave excitation force transfer function, the frequency-dependent added mass and the damping matrices based on the three-dimensional potential theory (Lee and Newman, 2006). The panel model used is presented in Fig. 4.

For the TLP floater alone, the equation of motion in the frequency domain can be written as:

$$(m + A(\omega))\ddot{x} + C(\omega)\dot{x} + Kx = F_{exc}(\omega) \quad (15)$$

where $A(\omega)$ is the added mass matrix, $C(\omega)$ is the damping matrix, K is the hydrostatic stiffness and $F_{exc}(\omega)$ is the first-order wave excitation force matrix and x here represents the arbitrary degree of freedom. To solve Eq. (15) in the time-domain, the convolution integral is introduced to account for the frequency-dependent added mass and damping forces

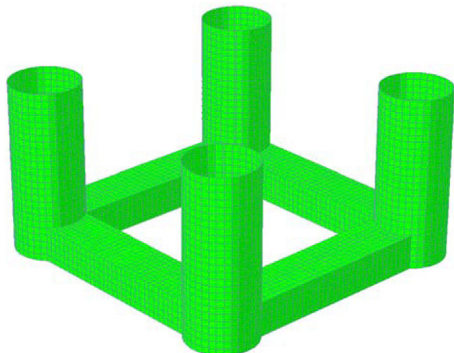


Fig. 4. Panel model of the TLP floater for hydrodynamic analysis.

(Reinholdtsen and Falkenberg, 2001). The equivalent form of Eq. (15) in time-domain is:

$$(m + A_{\infty})\ddot{x} + \int_{-\infty}^{\infty} h(t - \tau)\dot{x}(\tau)d\tau + Kx = F_{exc}(t) \quad (16)$$

where A_{∞} is the added mass matrix at an infinite excitation frequency and $h(\tau)$ is the retardation function, which is calculated by a transform of the frequency-dependent added mass or damping matrix, as given in Eq. (17). In general, $\int_{-\infty}^{\infty} h(t - \tau)\dot{x}(\tau)d\tau$, which combines the inertial and damping forces is termed hydrodynamic reaction force or radiation force.

$$h(\tau) = \frac{2}{\pi} \int_0^{\infty} C(\omega) \cos(\omega\tau) d\omega = -\frac{2}{\pi} \int_0^{\infty} \omega A(\omega) \sin(\omega\tau) d\omega \quad (17)$$

It should be noted that, in addition to the first-order wave force modelled by Eq. (16), there are also the second and the higher-order wave excitation force components under the irregular sea state. The second-order wave loads, which consist of contributions from each pair of regular wave components in the sea state, are quadratic with the wave amplitude and generally small in magnitude, especially considering relatively small significant wave heights in the fjord (less than 3 m with the return period of 100 years). The second-order wave loads consist of the mean drift force, the difference frequency (slow-varying drift) forces and the sum frequency forces (Faltinsen, 1993). It is known that the second and the higher-order wave forces are important, especially to the tendon/riser fatigue design. Considering the primary focus of this study is to propose a numerical framework for the global bridge response analysis, with emphasizes on the aerodynamic and hydrodynamic coupling and the inhomogeneous wave effect, it is reasonable to only include the mean drift force in the current stage. The other second-order wave load effects will be included in the numerical model in the future.

The wave excitation and the radiation forces in time-domain are applied in a specially developed, user-defined subroutine in Abaqus, which has been validated against the well-known commercial software SIMO (Reinholdtsen and Falkenberg, 2001). The hydrodynamic properties of the floater used in the validation study are from the same TLP as used in the floating bridge model, described in Table 2. Fig. 5 presents the comparison of the floater sway motion time histories under an irregular wave condition (Jonswap spectrum with $H_s = 2.4$ m; $T_p = 7.9$ s), where a good agreement is observed. This algorithm is therefore capable of evaluating the hydrodynamic loads for the floaters in time-domain.

Considering that the tethers stretch between the seabed and the position 50 m below the sea level, the wave excitation is neglected. The cross-sectional inertial and drag force on the tethers due to the ocean current are considered in Eq. (18):

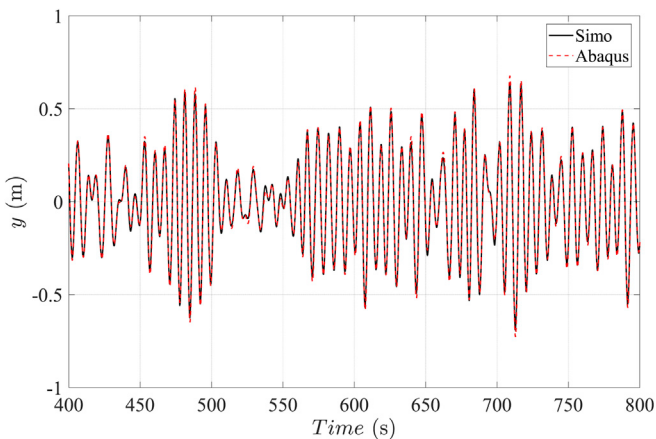


Fig. 5. Comparison of the floater sway motion under irregular waves ($H_s = 2.4$ m, $T_p = 7.9$ s) using Abaqus and SIMO, with floater characteristics given in Table 2.

$$F(t) = mC_a(-\dot{u}) + \frac{1}{2}\rho DC_D(U_c - u)|U_c - u| \quad (18)$$

where m is the mass of displaced fluid; ρ is the fluid density; D is the outer diameter of the tether; U_c is the ocean current velocity; u and \dot{u} are the tether velocity and acceleration in the current direction; C_a is the added mass coefficient and C_D is the drag coefficient.

3.3. Full bridge finite element model

As previously shown in Fig. 2, a finite element model of a floating bridge with the structural properties given in Table 1 is built in Abaqus, to represent the structural behaviour of the floating bridge. The bridge girder, the main cables, the hangers, the towers and the tethers are all modelled by the B31 beam element (2-node Timoshenko beam element with generalized cross-sectional properties) in Abaqus. There are around 3500 elements for the entire floating bridge model. The TLP is modelled as a rigid body with user-defined mass and stiffness elements, connecting the floating towers and the tethers. User-defined mass and stiffness elements are introduced to model the TLP's structural and hydrodynamic mass, mass moment of inertia and hydrostatic stiffness. The girder is partially fixed to the towers. The lateral (y), vertical (z) and torsional (r_x) girder degrees of freedom are rigidly linked to the crossbeams at the land-based towers. At the floating towers, the axial (x), lateral (y) and yaw (r_z) degrees of freedom are rigidly linked to the crossbeams but the vertical (z) and the torsional (r_x) motions are restricted by the hangers only.

Based on the numerical methodology proposed herein, the bridge dynamic response is solved by coupling bridge superstructure with the TLP and tether dynamics, under combined aero-hydrodynamic actions, implemented using a user-defined subroutine. The user-defined subroutine is established to calculate the instantaneous aerodynamic or hydrodynamic loads in six degrees of freedom, for all the load-bearing elements of the FE model. The developed subroutine primarily modifies the default subroutine "DLOAD" supported by Abaqus to calculate the element load at each time step, "URDFIL" is also called to obtain the element motion information for motion-dependent load calculation (ABAQUS, 2011). The implicit dynamic analysis using the Hilber-Hughes-Taylor time integration is adopted in Abaqus to solve the dynamic response of the whole system where the geometric nonlinearity is also considered. The Rayleigh damping model is used to account for the structural damping of the entire bridge, with a target of 0.5% of the critical damping, covering the first eigen-mode to the mode with the eigen-frequency of 5 Hz.

Table 5 summarizes different actions considered. In each case, the load time-series are generated with a duration of one-hour (as a short-term sea state realization) with a time step of 0.05 s.

4. Results and discussion

There are two main actions contributing to the global response of the floating bridge: i.e. aerodynamic and hydrodynamic loads. However,

Table 5
Summary of the aerodynamic and hydrodynamic loads for the floating bridge.

Aerodynamic actions	Wind	Quasi-steady buffeting loads and motion dependent loads; considering non-linear and coupling ^a terms
Hydrodynamic actions	Wave	Excitation force: Radiation force: Other forces: TLPs: Tethers:
		First order wave excitation force Added mass and damping force Mean drift force Mean drag force Inertial and drag forces
	Current	

^a Coupling here implies the interactions of the wind loads in lateral, vertical and torsional directions.

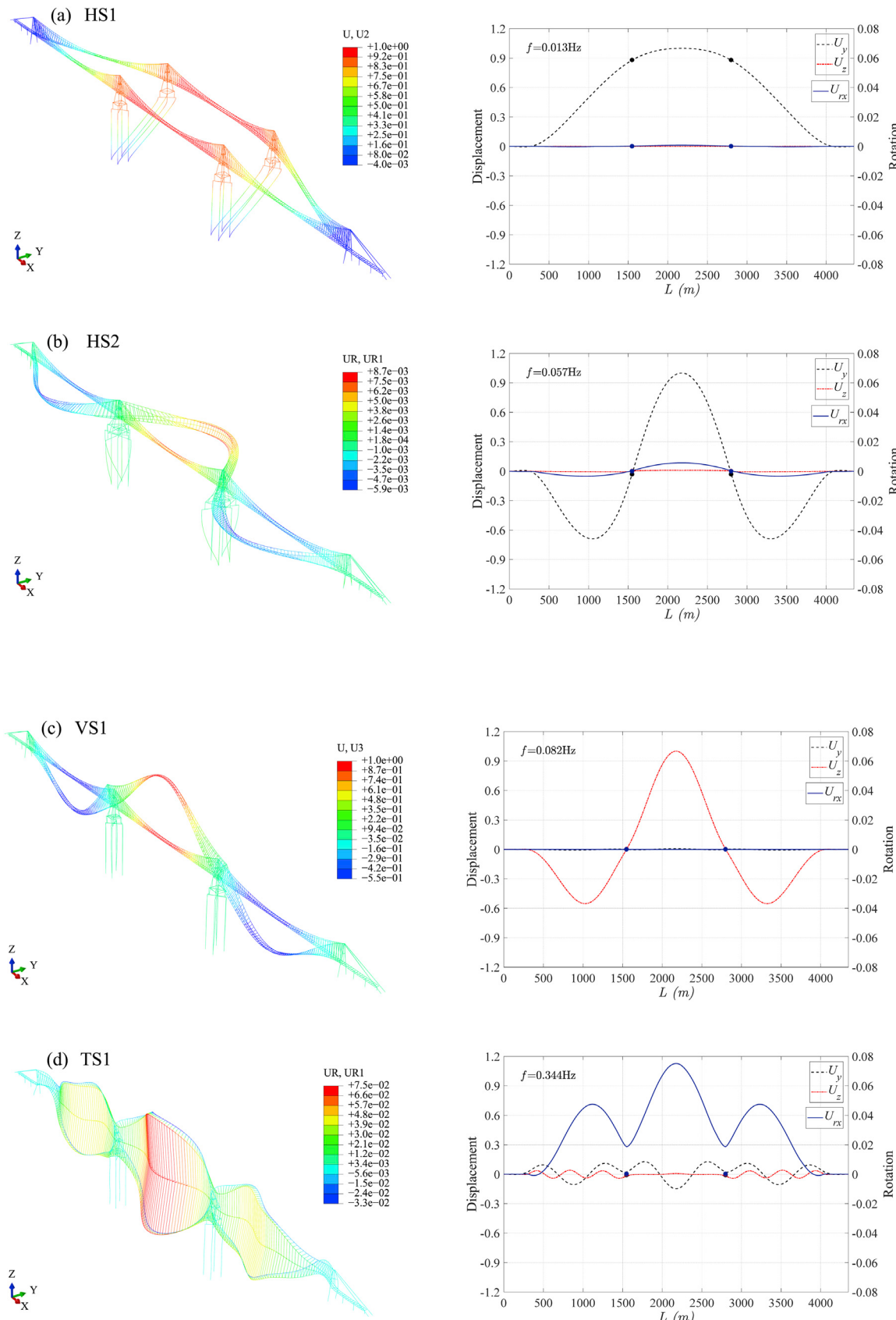


Fig. 6. Four representative symmetric eigen-modes of the Sulafjord bridge (left column: three-dimensional mode shapes of the bridge; right column: the relative modal displacements of the girder (lines) and TLPs (dots). Rotations are in radians associated with the translational displacements in meters).

until now, there is no numerical tool available to perform a fully coupled aerodynamic and hydrodynamic analysis of a long-span bridge structure in the time-domain, considering the inhomogeneity of environmental conditions. Some attempts to estimate the overall floating suspension bridge response have been made using a simplified modelling methodology, by calculating the bridge response separately for aerodynamic and hydrodynamic loads and then superimposing the two contributions (Nestebø et al., 2015). That is a commonly used approach for engineering problems when a fully coupled analysis is deemed unfeasible or the proper tools are unavailable (DNV, 2010).

In the following sections, the selected modal characteristics of the bridge are presented first. The fully coupled bridge response under combined wind, wave and current loads is then described. Numerical results considering the aerodynamic or hydrodynamic load separately are also discussed, with emphasis on the coupling effects and contributions from the different actions to the floating bridge response.

4.1. Modal bridge characteristics

Fig. 6 presents four eigen-modes of the bridge, i.e. the first and the second lateral symmetric modes HS1 and HS2, the first vertical symmetric mode VS1 and the first symmetric torsional mode TS1. The modes are denoted HS1, HS2, VS1 and TS1, according to the dominant response component. However, these modes also include the response components in other directions (mechanical modal coupling). For example, the lateral motion-dominated mode HS2 also involves the girder torsion, as shown in **Fig. 6(b)**. The modal displacements of the girder are coupled with the TLPs and tethers as well. For example, the TLPs' yaw motions are seen to be coupled with the girder lateral motion in **Fig. 6(b)**.

Fig. 7 presents the distribution of the first 500 eigen-frequencies computed, with a value below 2.4 Hz. The plot shows that there are around 122 modes below 0.5 Hz, which corresponds to the wind and wave excitation frequency range as marked in the plot. The four modes presented in **Fig. 6** are also marked in **Fig. 7** based on their eigen-frequency values.

4.2. Bridge response under combined aerodynamic and hydrodynamic loads

Fig. 8 presents the bridge response (mean value and standard deviation) under the combined action of wind, waves and current, with a return period of 100 years. The study case assumes different wave conditions at two TLPs (environmental condition 1 in **Table 3**). The bridge response is averaged over the five simulated cases. The response of the TLPs at the waterline level is also included in the plots for reference, as shown by the green triangles. The locations of the four towers are

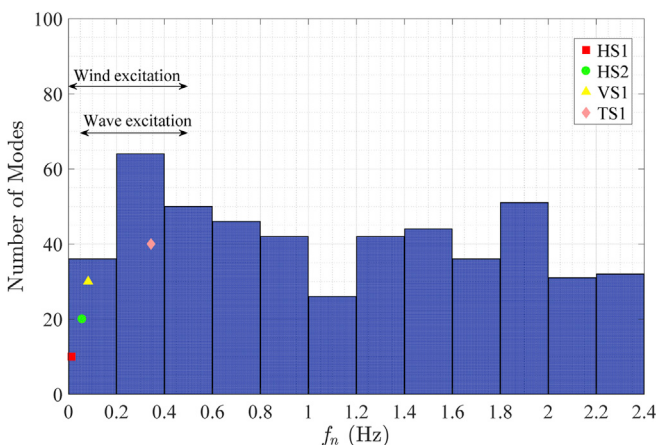


Fig. 7. Distribution of the first 500 eigen-frequencies, computed for the Sulafjord Bridge concept.

marked on the horizontal axis in each plot for reference. **Fig. 9** presents the power spectral density (PSD) of the girder displacement response, the spectra are based on the results from one of the five simulations. The PSDs are calculated using Welch's overlapped segment averaging estimator (MathWorks, 2005; Welch, 1967), where the time series are divided into 8 segments with 50% overlap and a Hamming window is used. The first five minutes of the results were not included in the PSD estimation, to avoid the transient state in the beginning of the simulations.

Fig. 8(a) presents the lateral mean displacement, with the largest mean displacement of about 30 m at mid-span. The maximum lateral displacement during the one-hour simulation among the five realizations is 45.7 m, which is quite a large value, mainly caused by the fact that the TLPs are compliant in the horizontal plane. However, considering the total length of the floating bridge between the two fixed towers is 3750 m, the maximum lateral girder displacement is around 1.2% of the total span length. Under these extreme conditions, the total mean tension of the tethers increased by about 25%, but the stress levels remain well within the operational range. The standard deviation of the lateral displacement in **Fig. 8 (b)** implies a combined contribution from the mode HS1 and HA1, which is confirmed by the PSD contour plot in **Fig. 9(a)** where the energy distribution reflects the absolute value of the mode shape. The contour plot provides complementary information to the standard deviation plot, where contributions from HS2, HS3 and even higher frequency modes are all visible. The conventional PSD plot at the bridge mid-span is presented in **Fig. 9(b)**, where different modes are identified showing clear mode coupling.

The mean vertical displacement response is relatively small, less than two meters, as shown in **Fig. 8(c)**. It is negative (downward motion) for most of the bridge. Considering that the wind, wave and current are aligned in the same direction (perpendicular to the bridge plane), the static (mean) deformation will follow the first symmetric mode shape, and the primary static deformation is in the lateral direction due to the mean wind load. For the mode HS1, there is a negative vertical modal displacement component. This is expected for a TLP-type floater and termed as “set-down”. The “set-down” is the kinematic coupling between the horizontal surge/sway motions and the vertical heave motions (DNV, 2010). Considering a mean horizontal offset of 25 m and a tether length of 400 m, the vertical translation of the TLP should be about 0.78 m downward, if the tether stretch, which is around 0.05 m, is neglected. **Fig. 8(c)** shows that the TLP has a mean vertical displacement of around −0.92 m. This indicates that the vertical component in HS1 has the largest contribution to the mean vertical motion of the bridge. The standard deviation of the vertical displacement in **Fig. 8(d)** is comparable in magnitude to the mean displacement. With reference to the mode shapes in **Fig. 6(b)** and **(c)**, the distribution of the vertical displacement standard deviation along the girder indicates a modal contribution of the mode HS2 or VS1. However, the vertical motion at the floating tower location is non-zero, which explains the participation of other modes according to the fact that the TLPs are stationary in the heave direction for mode VS1 in **Fig. 6(c)**. Vertical modes associated with the TLP heave motions are of much higher frequency due to the enormous pre-tension in the tethers. The PSD contour plot in **Fig. 9(c)** illustrates that it is the vertical components of the motion dominant low-frequency lateral modes that give the strongest contribution to the vertical response of the bridge. According to the PSD plot at the bridge mid-span in **Fig. 9(d)**, other spectral peaks for the higher vertical modes can be noted, beside the VS1 mode, due to a lower aerodynamic damping associated with these modes, compared to the VS1 mode. A minor coupling with the torsional mode TS1 is also identified. Furthermore, the eigen-modes indicate a considerable response participation from vertical modes and tether modes within the frequency range from 0.1 Hz to 0.4 Hz.

As previously mentioned, only the mean drift force term for the second order wave effect is considered in the current numerical simulations. Other terms, especially the sum frequency terms, could possibly cause resonant oscillations of the higher frequency modes, which could

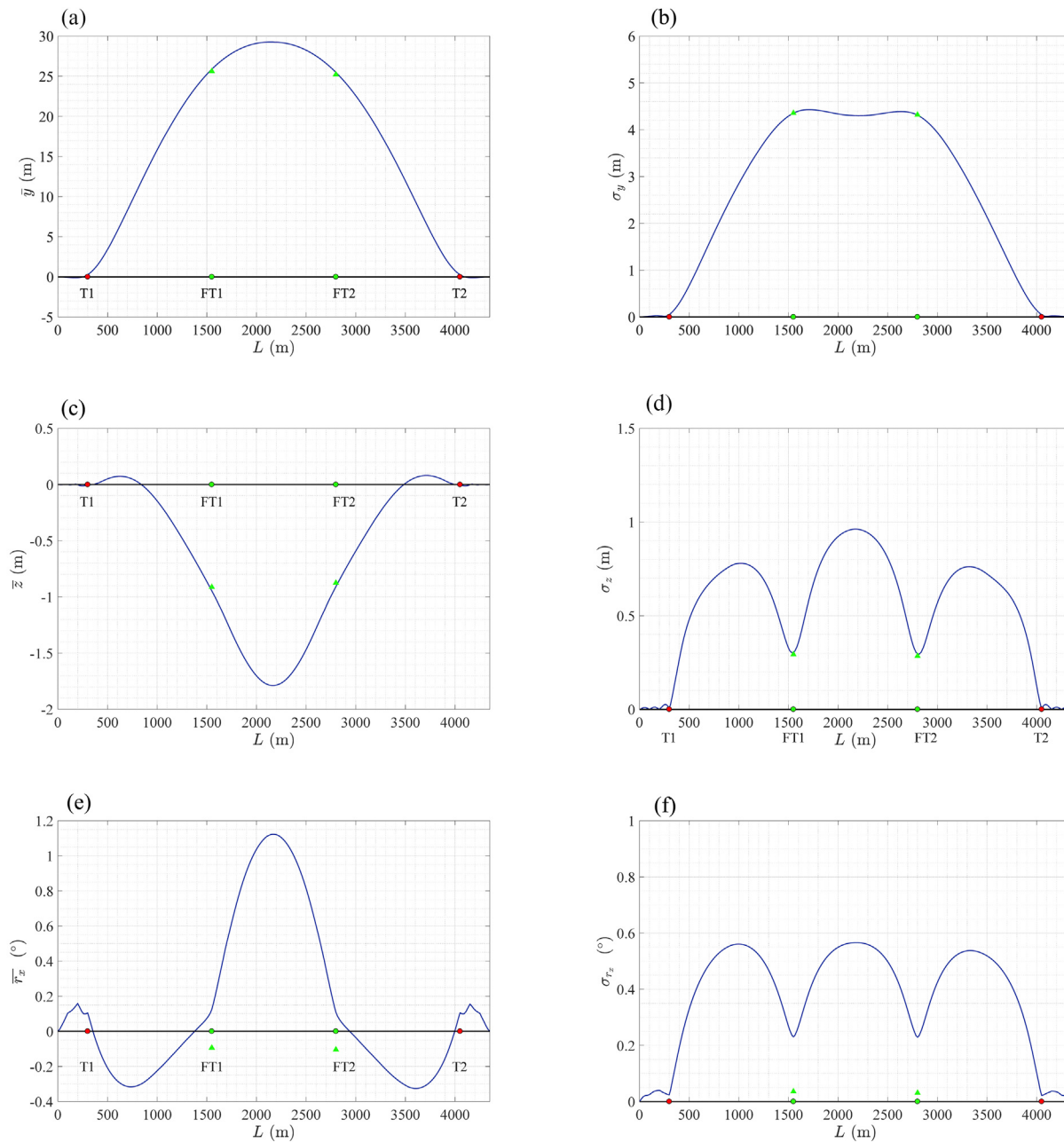


Fig. 8. Bridge girder displacement responses in lateral, vertical and torsional directions (left column: the mean displacement of the girder and TLPs; right column: the standard deviation of the displacement).

contribute to fatigue of the tethers. However, they are not likely to affect the global bridge response greatly due to the small amplitude of the second-order forces (Faltinsen, 1993).

The torsional mean response and the standard deviation are presented in Fig. 8(e) and (f). The corresponding vertical motion of the bridge deck edge due to the mean rotation at the bridge mid-span is about 26 cm. Although it is small, it may still be a cause of concern with regard to structural issues as well as traffic operations and human perception of motion, which will be studied in the future. Fig. 9(e) and (f) illustrate the frequencies, or modes of vibration that control the torsional motion. It is observed that the first three horizontal symmetric modes are highly coupled with the torsional motion. The standard deviation of the torsional response along the girder, shown in Fig. 8(f), agrees well with the torsional modal component in mode HS2 and the first torsional symmetric mode TS1, referring to Fig. 6(b) and (d). The PSD plots show that the contributions from the modes HS2 and TS1 are almost

comparable. According to the preliminary bridge design, the torsional degrees of freedom of the girder are not fixed to the floating towers in the finite element model. It is noticeable that the TLP roll motion (r_x) has an opposite mean value with respect to the bridge girder, as shown in Fig. 8(e). In the present case, it is uncertain whether this design is beneficial or not, which requires a further investigation on the constraints between the floating tower and the girder.

4.3. Contributions of aerodynamic and hydrodynamic loads to the bridge response

The contributions of different actions to the overall bridge response have been evaluated for four different “load combinations”:

- **Fully coupled:** Wind, wave and current loads applied in an integrated, coupled analysis;

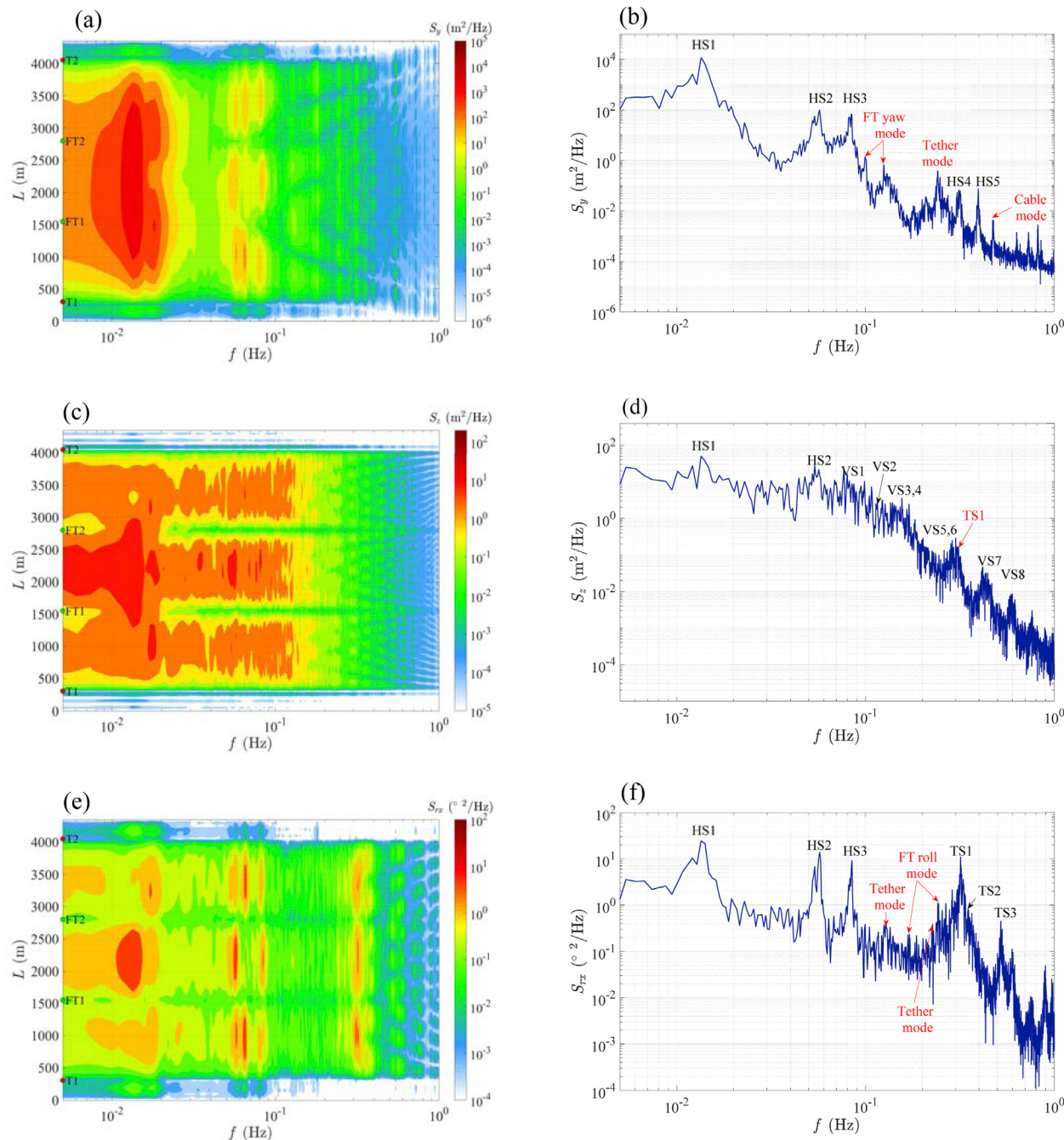


Fig. 9. Power spectral density of the girder displacement response in lateral, vertical and torsional directions (left column: the contour plot of the power spectral density along the whole bridge girder; right column: the power spectral density at the mid-span of the girder).

- *Aero only*: Buffeting wind loads acting on the bridge, accounting for the hydrodynamic radiation forces on the TLPs and tethers but no hydrodynamic excitation forces;
- *Hydro only*: Hydrodynamic loads on the TLPs and tethers only;
- *Aero + Hydro*: A linear superposition of the cases *Aero only* and *Hydro only*. The mean response is obtained by linearly summing the bridge response due to the aerodynamic and hydrodynamic actions; the standard deviation is obtained by calculating the square root of the variance sum, as denoted by $\sqrt{\sigma_i^2 + \sigma_j^2}$ in the legend of Fig. 10.

Fig. 10, presents the bridge response comparison for the four different load combinations, considering inhomogeneous waves at two TLPs based

on the averaged results from five realizations for environmental condition 1 in Table 3.

According to the comparisons in Fig. 10, the linear superposition of the mean displacement response seems to work reasonably well, especially for the lateral and torsional directions. However, this approach slightly underestimates the vertical mean displacement, with an underestimation of 13% at the midspan of the bridge. A careful examination of the results from the four different load combinations indicates that the two floating towers have a mean tilt (pitch direction r_y) towards each other under the static load. The tilt is slightly larger in the fully coupled case than if the linear superposition is applied, which potentially reduces the tension in the main cable and, therefore, leads to a smaller vertical stiffness for the bridge girder. Furthermore, the TLP floater is known to

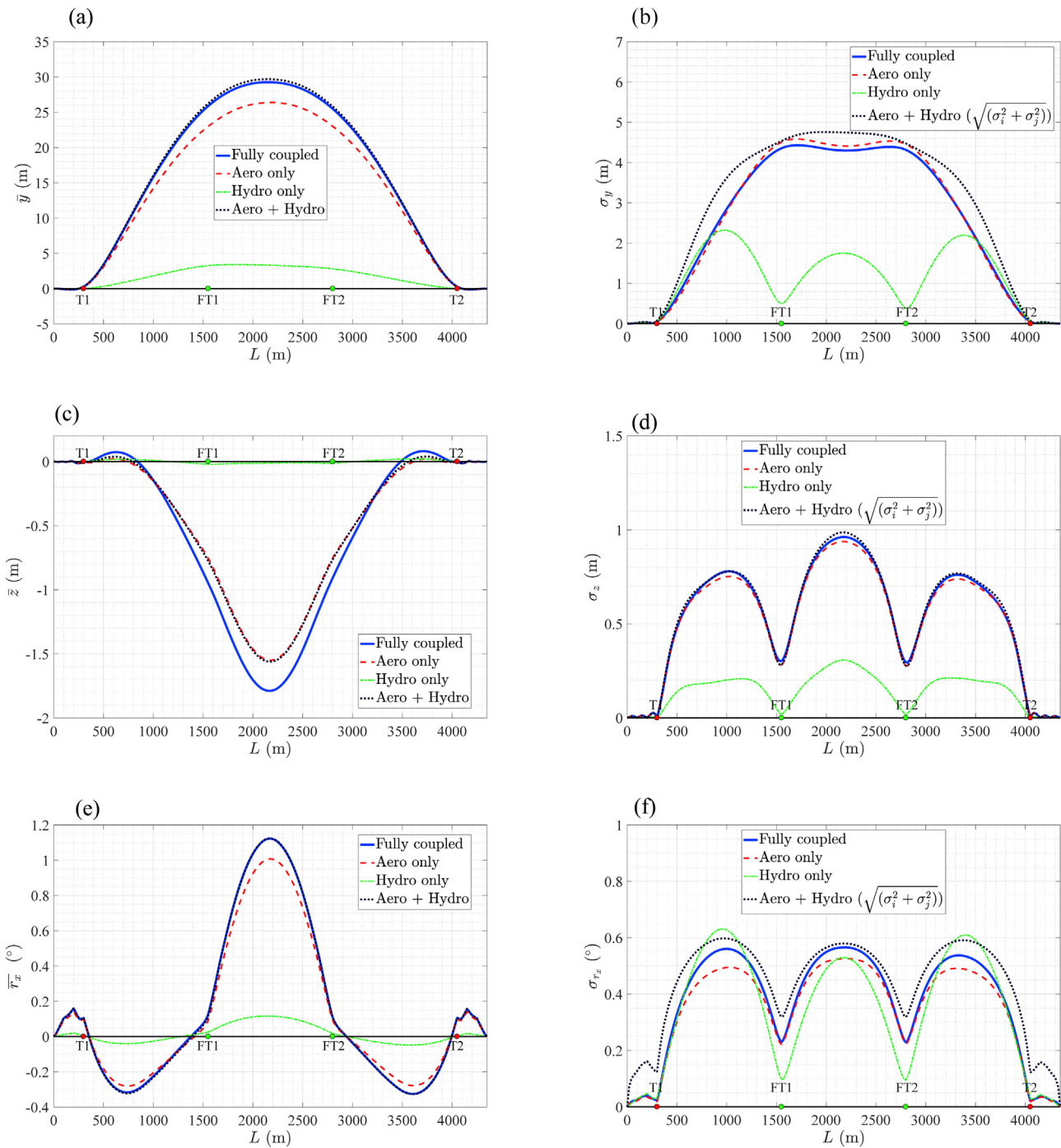


Fig. 10. Bridge girder response considering different load contributions, in lateral, vertical and torsional directions (left column: the mean displacement of the girder; right column: the standard deviation of the girder displacement).

have a non-linear restoring stiffness from the tethers in both the lateral and vertical directions. The vertical stiffness contributed by the tether pre-tension decreases with increasing lateral displacement. However, the lateral restoring stiffness increases under increasing lateral displacement, which is reflected in Fig. 10(a), showing that the linear superimposed mean lateral displacement slightly overestimates the coupled response.

For the standard deviation of the displacement response, the comparison with the fully coupled analysis demonstrates that a “linear superposition” agrees reasonably well with the fully coupled analysis. The agreement is especially good in the vertical direction in Fig. 10(d), with an overestimation of 3% for the maximum standard deviation at the

Table 6
Contribution of the aerodynamic loads to the bridge response at mid-span.

	\bar{y}	\bar{z}	\bar{r}_x	σ_y	σ_z	σ_{r_x}
Environmental condition 1	90.2%	86.6%	89.7%	102.5%	97.5%	93.0%
Environmental condition 2	89.5%	86.2%	89.2%	96.5%	90.8%	84.1%
Environmental condition 3	89.5%	86.1%	89.5%	96.4%	90.8%	83.9%

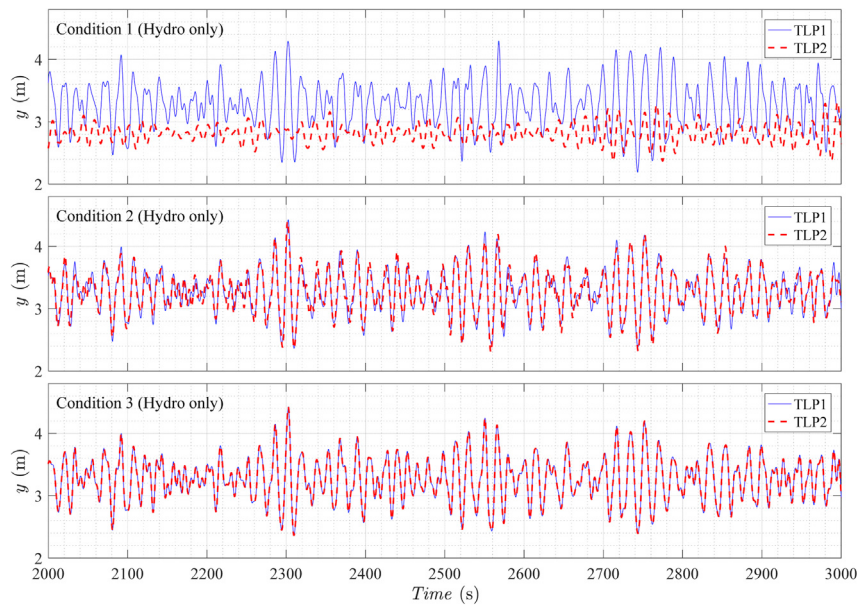


Fig. 11. Time histories of lateral displacement of the two TLPs for three different wave conditions under hydrodynamic action only.

midspan of the bridge. In the lateral and torsional directions, the bridge response by the “linear superposition” has some visible discrepancies compared to the fully coupled method, where the maximum standard deviation is overestimated by 11% and 7% respectively.

What's more, it seems that the “*Aero only*” case considering the hydrodynamic radiation effect has almost the same standard deviation level as the “*Fully coupled*” case for all the three directions. The dynamic response of the bridge for the environmental parameters considered is thus dominated by the aerodynamic action. The hydrodynamic forces acting on the two floating supports provide a limited excitation of the 4.3 km long structure. The hydrodynamic load effects are further attenuated by a significant aerodynamic damping in the extreme wind conditions studied, where the mean wind velocity at the girder level is about 50 m/s. Even if the second-order effects for the wave loading were considered, the aerodynamic actions on the global bridge response would still be dominant.

4.4. Effect of the inhomogeneity of the waves to the bridge response

According to Table 3, three different environmental conditions are considered, with different levels of the wave inhomogeneities. Table 6 summarizes the results from the “*Aero only*” cases normalized by the “*Fully coupled*” cases at the bridge mid-span. The comparison between environmental condition 1 and 3 indicates that the contribution from the aerodynamic action to the mean bridge response decreases slightly when the waves are homogeneously distributed, whereas the standard deviation of the displacement response is more affected by the inhomogeneity of the wave conditions. The contribution from the aerodynamic action to the lateral, vertical and the torsional dynamic response drops by 6%, 7% and 9% respectively when the waves are identical at two TLPs. The comparison between environmental condition 2 and 3 indicates that the absence of phase correlation of the wind-waves acting on the two floaters has a limited influence on the bridge response.

To further investigate the influence of the wave inhomogeneity on the floating bridge response, Fig. 11 presents the comparison of the lateral displacement time histories for the two TLPs under three different wave conditions when only hydrodynamic loads are acting on the floating bridge. The comparison for environmental condition 1 shows that TLP1 has a much larger static and dynamic lateral displacement response than TLP2 which is expected since the wave action is stronger at TLP1. For environmental condition 2, the displacement time histories are slightly

different due to the uncorrelated phases of the wind-sea components. This, on the other hand, suggests that the floating bridge is more sensitive to the swell conditions, which contain more energy at lower frequencies, corresponding to the dominant mode HS1. For environmental condition 3, the waves are identical at both TLPs which results in almost identical lateral responses.

5. Conclusions

The present study discusses a fully coupled time-domain analysis of a long multi-span bridge supported by two floating towers, including wind, wave and current loads. An ultimate limit state scenario considering environmental conditions with a return period of 100 years is used as a study case. The time-domain analysis is performed applying user-defined subroutines in Abaqus to account for loads due to the turbulent wind, irregular inhomogeneous waves and sheared ocean current. The wind action is described by adopting the quasi-steady buffeting theory including the frequency-independent motion-dependent forces, neglecting the cross-sectional aerodynamic admittance of the bridge deck. The wave action considered is based on potential theory, neglecting second order effects, and the action of the ocean currents is calculated according to the Morrison equation.

The finite element eigen-vibration analysis provides important modal information for the floating bridge, where significant mode coupling is observed. The results of the coupled analysis suggest that the bridge response under extreme conditions with a return period of 100 years is dominated by the low-frequency modes. For the extreme environmental conditions considered, the aerodynamic loads contribute to more than 80% of the bridge response. The contribution from the aerodynamic loads is more than 90% when considering inhomogeneous wave conditions. On the other hand, the contribution from the hydrodynamic loads on the floating towers is small, mainly because of limited significant wave heights in the fjord and the counteracting aerodynamic damping from the superstructure. Linear superposition of aerodynamic and hydrodynamic response from the uncoupled analyses gave a reasonable approximation of the mean response and the standard deviation of response.

The work presented herein aimed at providing a feasible numerical tool to design and analyse super-long span bridges proposed for several challenging fjord crossings in Norway. The fully coupled time-domain numerical model established enables us to assess the bridge response

due to complex environmental loads in a more accurate way than previously possible. As a recommendation for future research, an improved description of the local environmental conditions should be provided through a customized model for wind turbulence, wave and current profile considering the complex topography at the proposed bridge site. The higher-order hydrodynamic load effects should be included in future analyses, along with a more refined description of the self-excited aerodynamic forces. An updated bridge design, with top cables between the towers, will also be investigated.

Acknowledgement

This study is conducted as part of the research project “Wind-induced vibrations of long-span bridges” supported by Norwegian Public Roads Administration. The assistance by NPRA in providing the information on the floating bridge concept and the reference reports is gratefully acknowledged. The work performed by the former master students, Sondre Aspøy and Sindre Stensbak, on a separate finite element model of the bridge and the related wind-induced bridge response analyses have been of great value for the present study. We are also very grateful to Dr. Lin Li and Professor Sverre Haver for valuable discussions on the TLP hydrodynamics and the Sulafjord environmental conditions.

References

- Aas-Jakobsen, K., Strømmen, E., 2001. Time domain buffeting response calculations of slender structures. *J. Wind Eng. Ind. Aerod.* 89, 341–364.
- ABAQUS, 2011. ABAQUS documentation. Dassault Systèmes, Johnston, RI, USA.
- Bachynski, E.E., 2014. Design and Dynamic Analysis of Tension Leg Platform Wind Turbines. Norwegian University of Science and Technology, Trondheim, Norway.
- Bachynski, E.E., Moan, T., 2014. Ringing loads on tension leg platform wind turbines. *Ocean Eng.* 84, 237–248.
- Biety, J., Delaunay, D., Conti, E., 1995. Comparison of full-scale measurement and computation of wind effects on a cable-stayed bridge. *J. Wind Eng. Ind. Aerod.* 57, 225–235.
- Borge, J., Potac, J., Vaardal-Lunde, J., Thiis, T., 2015. Report: Preliminary Metocean Design Basis Sulafjorden. Multiconsult, Tromsø, Norway.
- Borri, C., Höffer, R., Zahlten, W., 1995. A nonlinear approach for evaluating simultaneous buffeting and aeroelastic effects on bridge decks. In: Proceedings of the Ninth International Conference on Wind Engineering. Wiley Eastern Limited, New Delhi, pp. 839–850.
- Chen, X., Matsumoto, M., Kareem, A., 2000. Time domain flutter and buffeting response analysis of bridges. *J. Eng. Mech.* 126, 7–16.
- Cheynet, E., Jakobsen, J.B., Snaebjörnsson, J., 2016. Buffeting response of a suspension bridge in complex terrain. *Eng. Struct.* 128, 474–487.
- Cheynet, E., Jakobsen, J.B., Snaebjörnsson, J., Mann, J., Courtney, M., Lea, G., Svartdal, B., 2017. Measurements of surface-layer turbulence in a wide Norwegian fjord using synchronized long-range Doppler wind lidars. *Rem. Sens.* 9, 977.
- Costa, C., Borri, C., Flaman, O., Grillaud, G., 2007. Time-domain buffeting simulations for wind–bridge interaction. *J. Wind Eng. Ind. Aerod.* 95, 991–1006.
- Davenport, A.G., 1961. The application of statistical concepts to the wind loading of structures. *Proc. Inst. Civ. Eng.* 19, 449–472.
- Diana, G., Resta, F., Rocchi, D., 2008. A new numerical approach to reproduce bridge aerodynamic non-linearities in time domain. *J. Wind Eng. Ind. Aerod.* 96, 1871–1884.
- DNV, 2010. RP-F205: Global Performance Analysis of Deepwater Floating Structures. Det Norske Veritas, DNV, Høvik.
- DNV, 2011. OS-C105: Structural Design of TLPS. DNV Services, Research and Publications, Hovik, Norway.
- DNV, G., 2014. DNV-RP-C205: Environmental Conditions and Environmental Loads. Det Norske Veritas AS, Oslo.
- Faltinsen, O., 1993. Sea Loads on Ships and Offshore Structures. Cambridge university press.
- Faltinsen, O., Newman, J., Vinje, T., 1995. Nonlinear wave loads on a slender vertical cylinder. *J. Fluid Mech.* 289, 179–198.
- Farr, T.G., Rosen, P.A., Caro, E., Crippen, R., Duren, R., Hensley, S., Kobrick, M., Paller, M., Rodriguez, E., Roth, L., 2007. The shuttle radar topography mission. *Rev. Geophys.* 45.
- Fenerci, A., Øiseth, O., 2017. Measured buffeting response of a long-span suspension bridge compared with numerical predictions based on design wind spectra. *J. Struct. Eng.* 143, 04017131.
- Gurley, K.R., Kareem, A., 1998. Simulation of ringing in offshore systems under viscous loads. *J. Eng. Mech.* 124, 582–586.
- Hasselmann, K., Barnett, T.P., Bouws, E., Carlson, H., Cartwright, D.E., Enke, K., Ewing, J.A., Gienapp, H., Hasselmann, D.E., Kruseman, P., Meerburg, A., Müller, P., Olbers, D.J., Richter, K., Sell, W., Walden, H., 1973. Measurements of wind wave growth and swell decay during the joint North sea wave project (JONSWAP). *Dtsch. Hydrogr. Z.* 8, 95.
- HYDRO, D., 2005. Wave Load& Stability Analysis of Fixed and Floating Structures. Det Norske Veritas, Norway.
- Jonkman, J., Kilcher, L., 2012. TurbSim User's Guide: Version 1.06. 00. National Renewable Energy Laboratory (Technical Report).
- Kim, M., Tahar, A., Kim, Y., 2001. Variability of TLP motion analysis against various design methodologies/parameters. In: The Eleventh International Offshore and Polar Engineering Conference. International Society of Offshore and Polar Engineers.
- Lee, C.-H., Newman, J.N., 2006. WAMIT User Manual. WAMIT, Inc.
- Lie, H., Fu, S., Fylling, I., Fredriksen, A.G., Bonnemaire, B., Kjersem, G.L., 2016. Numerical modelling of floating and submerged bridges subjected to wave, current and wind. In: ASME 2016 35th International Conference on Ocean, Offshore and Arctic Engineering. American Society of Mechanical Engineers pp. V007T006A075–V007T006A075.
- Lin, Y., Yang, J., 1983. Multimode bridge response to wind excitations. *J. Eng. Mech.* 109, 586–603.
- Macdonald, J.H., 2003. Evaluation of buffeting predictions of a cable-stayed bridge from full-scale measurements. *J. Wind Eng. Ind. Aerod.* 91, 1465–1483.
- Marino, E., Nguyen, H., Lugni, C., Manuel, L., Borri, C., 2015. Irregular nonlinear wave simulation and associated loads on offshore wind turbines. *J. Offshore Mech. Arctic Eng.* 137, 021901.
- Masciola, M.D., 2011. Dynamic Analysis of a Coupled and an Uncoupled Tension Leg Platform. McGill University (Canada).
- MathWorks, I., 2005. MATLAB: the Language of Technical Computing. Desktop Tools and Development Environment, Version 7. MathWorks.
- Nestebø, A., Bonnemaire, B., Buckholm, P., Fredriksen, A., 2015. Feasibility Study Crossing of Sulafjorden. Multiconsult, Oslo, Norway.
- Paulsen, B.T., Bredmose, H., Bingham, H.B., Jacobsen, N.G., 2014. Forcing of a bottom-mounted circular cylinder by steep regular water waves at finite depth. *J. Fluid Mech.* 755, 1–34.
- Petrauskas, C., Liu, S., 1987. Springing force response of a tension leg platform. In: Offshore Technology Conference. Offshore Technology Conference.
- Reinholdtsen, S., Falkenberg, E., 2001. SIMO—theory/user Manual. MT51 F93–0184. MARINTEK.
- Samferdselsdepartement, D.K., 2017. Meld. St. 33 Nasjonal Transportplan 2018–2029 (Oslo, Norway).
- Scanlan, R., 1978. The action of flexible bridges under wind, II: buffeting theory. *J. Sound Vib.* 60, 201–211.
- Shinozuka, M., Deodatis, G., 1991. Simulation of stochastic processes by spectral representation. *Appl. Mech. Rev.* 44, 191–204.
- Svensson, H., Kovacs, I., 1992. Examples of analytical aerodynamics investigations of long-span bridges. In: Aerodynamics of Large Bridges: Proceedings of the First International Symposium on Aerodynamics of Large Bridges (Copenhagen, Denmark).
- Vegvesen, S., 2015. In: Vegdirektoratet (Ed.), Håndbok N400 Bruprosjektering.
- Wang, H., Li, A., Hu, R., 2010. Comparison of ambient vibration response of the Runyang Suspension Bridge under skew winds with time-domain numerical predictions. *J. Bridge Eng.* 16, 513–526.
- Wang, J., Cheynet, E., Jakobsen, J.B., Snaebjörnsson, J., 2017. Time-domain analysis of wind-induced response of a suspension bridge in comparison with the full-scale measurements. In: Proceedings of the Proceedings of the ASME 2017 36th International Conference on Ocean, Offshore and Arctic Engineering, OMAE2017–61725.
- Wei, W., Fu, S., Moan, T., Lu, Z., Deng, S., 2017. A discrete-modules-based frequency domain hydroelasticity method for floating structures in inhomogeneous sea conditions. *J. Fluid Struct.* 74, 321–339.
- Welch, P., 1967. The use of fast Fourier transform for the estimation of power spectra: a method based on time averaging over short, modified periodograms. *IEEE Trans. Audio Electroacoust.* 15, 70–73.
- Xu, Y., Zhu, L., 2005. Buffeting response of long-span cable-supported bridges under skew winds. Part 2: case study. *J. Sound Vib.* 281, 675–697.